BIOCHEMISTRY

Revisiting the concept of peptide bond planarity in an iron-sulfur protein by neutron structure analysis

Yuya Hanazono[1,2]†, Yu Hirano[2,3], Kazuki Takeda[1], Katsuhiro Kusaka[4], Taro Tamada[2]*, Kunio Miki[1]*

The planarity of the peptide bond is important for the stability and structure formation of proteins. However, substantial distortion of peptide bonds has been reported in several high-resolution structures and computational analyses. To investigate the peptide bond planarity, including hydrogen atoms, we report a 1.2-Å resolution neutron structure of the oxidized form of high-potential iron-sulfur protein. This high-resolution neutron structure shows that the nucleus positions of the amide protons deviate from the peptide plane and shift toward the acceptors. The planarity of the H—N—C═O plane depends strongly on the pyramidalization of the nitrogen atom. Moreover, the orientation of the amide proton of Cys^{75} is different in the reduced and oxidized states, possibly because of the electron storage capacity of the iron-sulfur cluster.

INTRODUCTION

Peptide bonds are amide bonds that are generated by the dehydration reaction between α–amino acids in proteins. The C—N bond has a partial double-bond character because of its resonance stabilization with a separation of charge between the nitrogen and oxygen atoms (*1*), and thus the bond is energetically most stable when the six atoms that constitute the peptide group are in the same plane. The partial double-bond character is important for resistance to hydrolysis (*2*) and forming secondary structures (*3*–*5*). The amide hydrogen and oxygen atoms in the peptide bond often act as donors and acceptors in hydrogen bonds, respectively. Hydrogen bonds between nitrogen and oxygen atoms are typically 2.5 to 3.5 Å, and the energy of an N—H…O═C hydrogen bond contributes about 1 to 10 kcal/mol to protein stability (*6*–*9*). The strength of hydrogen bonds in proteins depends on bond length, bond angle, polarity, pressure, and temperature, among other parameters (*10*–*14*). Despite the partial double-bond character of peptide bonds, several high-resolution x-ray structures and computational analyses have shown the distortion of the ω angle, which describes the $C_{\alpha i-1}$—C_{i-1}—N_i—$C_{\alpha i}$ plane, where *i* is the residue number (*15*–*17*). The peptide bond is not perfectly planar in these structures, and the distortion depends on the φ angle, which describes the C_{i-1}—N_i—$C_{\alpha i}$—C_i plane, and the ψ angle, which describes the N_i—$C_{\alpha i}$—C_i—N_{i+1} plane (*15*, *17*, *18*). The deviations of the position of the amide protons from the peptide plane are not well understood because of the lack of structural data for hydrogen atoms, and only a few neutron structures and nuclear magnetic resonance (NMR) analyses have revealed the deviations of these protons (*19*–*21*). Neutron crystallography is a powerful method for directly detecting the position of hydrogen atoms, because the magnitudes of the coherent scattering lengths of protium and deuterium atoms are comparable to that of carbon (*22*). Moreover, high-resolution neutron structures can determine the precise locations of hydrogen nuclei, which are different from the center of electron density because of polarization.

High-potential iron-sulfur protein (HiPIP) is responsible for electron transfer from cytochrome bc_1 complex to light-harvesting–reaction center complexes (LH1-RC) in bacterial photosynthesis (*23*). HiPIP has a cubane-like Fe_4S_4 cluster at its center, with a redox potential of above +300 mV (*24*). This high potential arises from the hydrogen bonds and hydrophobic environment around the iron-sulfur cluster (*25*–*27*). The Fe_4S_4 cluster is divided into two Fe_2S_2 clusters; subcluster 1 (Fe_1-S_4-Fe_2-S_3) and subcluster 2 (Fe_3-S_1-Fe_4-S_2). In HiPIP, subcluster 1 is largely responsible for electron storage (*28*). We have previously reported the x-ray crystal structures of reduced (~0.48-Å resolution) and oxidized (~0.80-Å resolution) HiPIP from a thermophilic purple bacterium, *Thermochromatium tepidum* (*28*–*33*). The ultrahigh-resolution x-ray structure at 0.48-Å resolution in the reduced state revealed large distortions of the peptide bonds around the iron-sulfur cluster (*28*). Moreover, some electron densities of amide protons deviated from the peptide plane. Although the electron density of hydrogen atoms is detected in the high-resolution x-ray structure of HiPIP, the neutron structure is important to determine the precise locations of hydrogen nuclei to elucidate the effect of hydrogen bonds on the redox potential and reaction mechanism.

RESULTS AND DISCUSSION

X-ray/neutron joint refinement of oxidized HiPIP

We collected x-ray and neutron diffraction data of oxidized HiPIP at 0.66- and 1.2-Å resolution, respectively, from the same crystal at a cryogenic temperature of 100 K (fig. S1 and table S1). Initially, we performed the x-ray structure refinement and subsequently determined the coordinates of hydrogen atoms using neutron diffraction data (table S2). The final R_{work} and R_{free} are 7.41 and 8.15% for the x-ray data and 15.4 and 16.8% for the neutron data, respectively. There are no major structural differences compared with the 0.48-Å resolution structure in the reduced state (fig. S2A). These structures can be superimposed with a root mean square deviation for all the nonhydrogen polypeptide atoms of 0.62 Å. The ω angles are also identical between the two states, including the highly distorted

[1]Department of Chemistry, Graduate School of Science, Kyoto University, Sakyo-ku, Kyoto 606-8502, Japan. [2]Institute for Quantum Life Science, National Institutes for Quantum Science and Technology, Tokai, Ibaraki 319-1106, Japan. [3]JST, PRESTO, Kawaguchi, Saitama 332-0012, Japan. [4]Frontier Research Center for Applied Atomic Sciences, Ibaraki University, Tokai, Ibaraki 319-1106 Japan.
*Corresponding author. Email: miki@kuchem.kyoto-u.ac.jp (K.M.); tamada.taro@qst.go.jp (T.T.)
†Present address: Medical Research Institute, Tokyo Medical and Dental University, Bunkyo-ku, Tokyo 113-8510, Japan.

peptide bond around the iron-sulfur cluster (fig. S2B). The CN bond lengths have a negative correlation with the CO bond lengths (fig. S2C and table S3), as observed in other high-resolution structures (*34*). These bond lengths indicate the degree of the double-bond character of the peptide bond. In the electron and neutron scattering length (or nuclear) densities, each of the atoms, including hydrogen atoms, can be observed separately (Fig. 1A). The nuclear densities of D and $D_{\gamma 1}$ of Thr^{13} around the protein surface are observed to be positive because of hydrogen (protium)–deuterium (H/D) exchange. In contrast, the nuclear density of H of Val^{71}, which is buried in a hydrophobic core, is negative. The protonation states of ionizable residues correspond to the differences in the CO bond lengths (fig. S3). The centers of the electron and nuclear densities of hydrogen atoms are different because of the polarization (Fig. 1, B and C). The neutron diffraction data of oxidized HiPIP are high quality enough to determine the precise locations of the hydrogen nuclei.

Distortion of the amide proton

The bond lengths and angles for hydrogen atoms are generally constrained in the x-ray and neutron structural refinement as a riding model. However, the nuclear densities of the amide protons of oxidized HiPIP deviate from the peptide plane (Fig. 2A). Therefore, the coordinates of amide protons whose occupancies are greater than or equal to 0.60 of deuterium or 0.75 of protium, the nuclear density of which was clearly observed, were refined without geometry restraints. In addition, the deuterium atoms of side chains in a single conformation were also refined. The coordinates of 64 amide protons and 36 deuterium atoms on the side chains were refined without restraints. The data-to-parameter ratio of the neutron diffraction data was sufficient to refine the coordinates of the amide protons. The refined hydrogens fit well into the omit map (Fig. 2A). The hydrogen bond patterns of the refined amide protons are shown in tables S4 and S5. A hydrogen bond usually consists of a single acceptor and donor pair. However, a hydrogen bond pattern can sometimes contain more than one donor or acceptor and is called as a bifurcated hydrogen bond. To understand the effect of the bifurcated hydrogen bonds, we divided the amides into those with a clear single acceptor (table S4) and those with two acceptors near the amide proton (table S5). In single-acceptor hydrogen bonds, most of the donor-hydrogen-acceptor refined angles (∠DH…A) are greater than those of the riding model (Fig. 2B and table S4). The positions of the nuclei of the amide protons shift toward the acceptor atoms (Fig. 2A). In bifurcated hydrogen bonds, some amide protons (Ala^{14}, Ile^{15}, Ala^{32}, Gly^{35}, Trp^{58}, and Gly^{60}) point away from the nearest acceptor atoms (Fig. 2C and table S5). These hydrogen atoms are attracted from two directions by the electrostatic force, and the N—H bond is shorter than the ideal value of 1.02 Å obtained from neutron scattering or NMR studies (*35*, *36*). The N—H bond length is critically affected by the strength of the hydrogen bond, which depends mainly on the donor-acceptor distance and angle (*37*). The bonding energy of the bifurcated hydrogen bonds is slightly smaller than that of the single-acceptor hydrogen bond (*38*). Therefore, it is likely that the length of the N—H bond in the bifurcated hydrogen bonds is short. Only the amide proton of Asn^{70} points away from the nearest acceptor atom, although there are no other acceptor atoms nearby. S_γ of Cys^{43} is 4.62 Å from the amide proton of Asn^{70} (fig. S4), which may affect the position of the amide proton of Asn^{70}. The refined ∠DH…A of three of the four cysteine residues covalently bound to the iron-sulfur cluster (Cys^{43}, Cys^{61}, and Cys^{75}) deviate substantially from the riding model (table S3). This deviation is correlated with the distortion of the ω angles caused by the Fe—S_γ bonds between the iron-sulfur cluster and the cysteine residues (fig. S2B). Although most of the N—H bond lengths are around the ideal value of 1.02 Å, some of the N—H bond lengths deviate from the ideal value (Fig. 2D). The hydrogen bonds between the amide protons and S_γ of the cysteine residues that are bound to the iron-sulfur cluster (Leu^{63} and Ser^{77}) change the N—H bond length substantially (table S4). Pyramidalization at the peptide nitrogen atom is observed because of the attraction of hydrogen atoms by acceptor atoms and the distortion of the ω angle (fig. S5A). The degree of nitrogen pyramidalization (θ_N), which is the dihedral angle between the C_{i-1}—N_i—H_i and C_{i-1}—N_i—$C_{\alpha i}$ planes, does not show a clear correlation with the C—N length [correlation coefficient (r) = 0.23] (fig. S5B). This result indicates that the change in the double-bond character of the peptide bond is not decisive for the nitrogen pyramidalization. In general, the planarity of the peptide bond is discussed by referring to the ω angles due to the insufficient structural data for the amide protons. In this study, we focus on the planarity of the H_i—N_i—C_{i-1}=O_{i-1} planes in the peptide bond

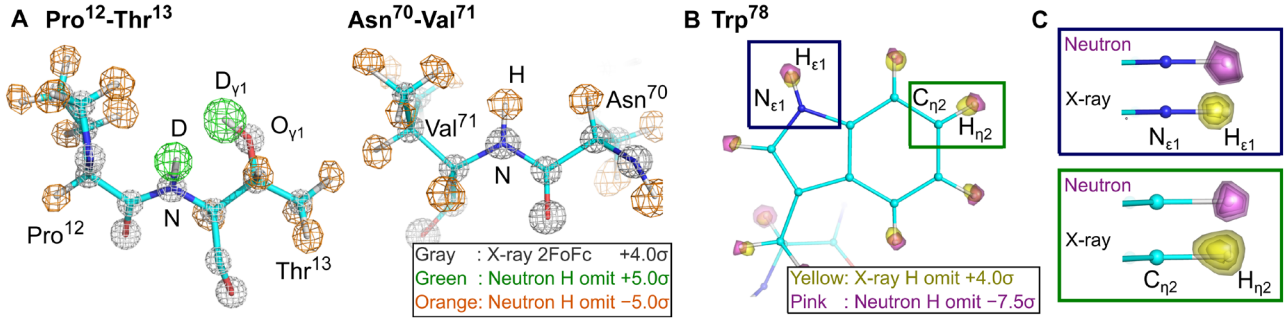

Fig. 1. Electron and nuclear density maps of oxidized HiPIP. (**A**) Electron and nuclear density maps around the peptide bond between Pro^{12} and Thr^{13} and between Asn^{70} and Val^{71}. The $2F_{obs} - F_{calc}$ electron density map is shown in gray at a contour level of +4σ. The $F_{obs} - F_{calc}$ hydrogen omit nuclear density map is shown in green and orange at a contour level of +5σ and −5σ, respectively. (**B**) Difference between the center of electron density and nuclear density of the indole ring of Trp^{78}. The $F_{obs} - F_{calc}$ hydrogen omit electron density map and $F_{obs} - F_{calc}$ hydrogen omit nuclear density map are shown in yellow (+4σ) and pink (−7.5σ), respectively. (**C**) Close-up view of $N_{\varepsilon 1}$—$H_{\varepsilon 1}$ and $C_{\eta 2}$—$H_{\eta 2}$ of Trp^{78}. The $F_{obs} - F_{calc}$ hydrogen omit electron density map and $F_{obs} - F_{calc}$ hydrogen omit nuclear density map are shown in yellow (+4.5σ, +4σ, and +3.5σ) and pink (−8σ, −7.5σ, and −7σ), respectively.

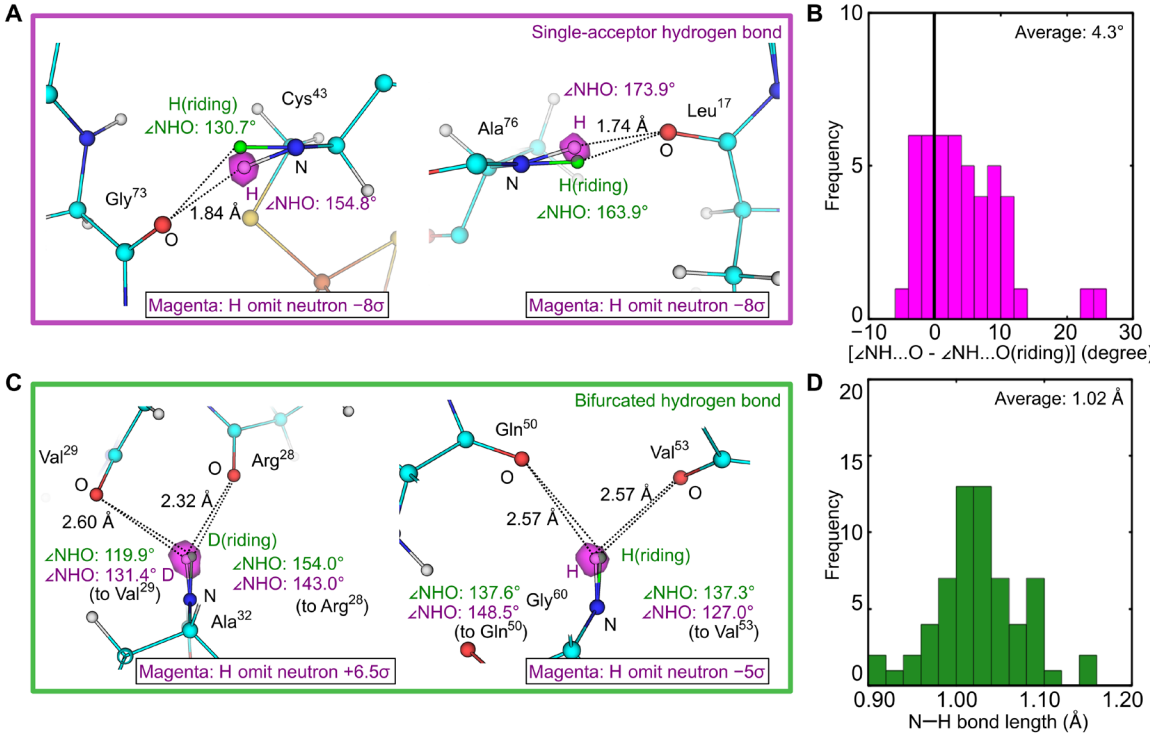

Fig. 2. Distortion of the peptide bond. (**A**) Deviations of hydrogen atoms from the peptide plane. The $F_{obs} - F_{calc}$ hydrogen omit nuclear density map is shown in magenta. The amide hydrogen atoms of riding models are shown in green. The distance between amide hydrogen and oxygen atoms are shown in black. The angles of NH…O for experimentally determined models and riding models are shown in magenta and green, respectively. (**B**) Histogram of the frequency of differences in donor-hydrogen acceptor angles in single-acceptor hydrogen bonds between the experimentally refined model and the riding model. (**C**) Deviations of hydrogen atoms from the acceptor atoms in bifurcated hydrogen bonds. (**D**) Histogram of the frequency of N—H bond lengths for amide protons.

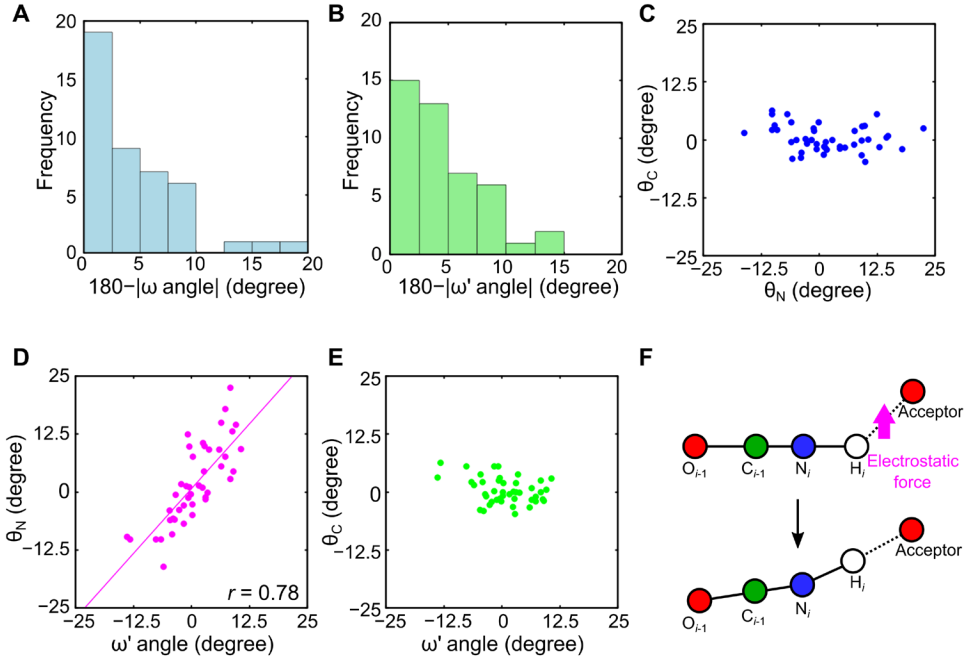

Fig. 3. Position of hydrogen and oxygen atoms in the peptide bond. (**A**) Histogram of the frequency of the deviation from the plane of the ω angle. The peptide bonds including the refined amide protons are counted. (**B**) Histogram of the frequency of the deviation from the plane of the dihedral angle of H_i—N_i—C_{i-1}═O_{i-1} (ω′ angle). (**C**) Scatter plot of θ_C against θ_N. (**D**) Scatter plot of θ_N against ω′ angle. Linear regression is shown as a solid line. (**E**) Scatter plot of θ_C against the ω′ angle. (**F**) Side-view schematic of the peptide bond. The attraction of the amide proton by the acceptor atom shifts the H_i—N_i—C_{i-1}═O_{i-1} plane.

because we refined the amide protons without geometry restraints. The dihedral angle of H_i—N_i—C_{i-1}=O_{i-1} is defined as the ω′ angle. The distributions of the ω angle and ω′ angle have σ of 6.1° and 5.7°, respectively (Fig. 3, A and B). The degree of carbon pyramidalization (θ_C) ranges from about −5° to 5° from the plane, whereas θ_N ranges from −20° to 25° (Fig. 3C). θ_C is much smaller because the oxygen atoms must rotate simultaneously with the $C_{\alpha i-1}$—C_{i-1}—N_i plane due to the sp^2 hybridization of the C_{i-1} atom. There is a correlation between θ_N and the ω′ angle (r = 0.78) (Fig. 3D). In contrast, there is no clear correlation between θ_C and the ω′ angle (Fig. 3E). The planarity of the H_i—N_i—C_{i-1}=O_{i-1} plane depends strongly on the pyramidalization of the nitrogen atom. In other words, the attraction of amide protons by acceptor atoms determines the planarity of the H_i—N_i—C_{i-1}=O_{i-1} plane (Fig. 3F).

In arginine residues, the guanidino group can deviate from the ideal conformation (*39*). In HiPIP, two arginine residues (Arg^{28} and Arg^{33}) are present on the protein surface. In Arg^{28}, the N_ε—C_ζ, C_ζ—$N_{\eta1}$, and C_ζ—$N_{\eta2}$ bond lengths are similar (table S6). In contrast, in Arg^{33}, the N_ε—C_ζ, and C_ζ—$N_{\eta1}$ bond lengths are shorter than the C_ζ—$N_{\eta2}$ bond length. In addition, the C_δ atom of Arg^{33} deviates from the guanidinium plane, whereas the C_δ atom of Arg^{28} does not (fig. S6, A and B). Thus, the planarity of the guanidino group is affected by the surrounding conditions. In addition, nitrogen pyramidalization of the $N_{\eta1}$ and $N_{\eta2}$ atoms is observed (fig. S6, C and D). The hydrogen atoms in the guanidino group also shift toward the acceptor atoms. Nitrogen pyramidalization in the guanidino group has already been reported in the neutron structure of photoactive yellow protein (*40*); thus, pyramidalization in the arginine residues may be common in proteins.

Amide protons around the iron-sulfur cluster that is involved in electron transfer

The distances and angles including hydrogen atoms around the iron-sulfur cluster are shown in table S7. In the oxidized state, the distances between the sulfur atoms and hydrogen bond donors are slightly longer. This elongation indicates that all sulfur atoms undergo a change in electronic state caused by oxidation and follows the same trend as in our previous study of the x-ray structures at 0.8-Å resolution (*32*). In the redox protein, the hydrogen atoms that are coordinated to sulfur atoms play a major role in redox potential (*26*, *41*, *42*). The four amide protons interact with the sulfur atoms of the cysteine residues covalently bound to the Fe atoms (Fig. 4A). The two amide protons of Phe^{48} and Thr^{79} interact with the sulfur of Cys^{46}, which is bound to subcluster 1, and the amide protons of Leu^{66} and Ser^{77} interact with the sulfur atoms of Cys^{61} and Cys^{75}, respectively, which are bound to subcluster 2. The NH bond lengths of 0.97 Å of Phe^{48} and 1.02 Å of Thr^{79} are shorter than or equal to the ideal value of 1.02 Å (*35*, *36*), whereas the NH bond lengths of 1.14 Å of Leu^{63} and 1.15 Å of Ser^{77} are substantially longer. Because the hydrogen bonds coordinating to the sulfur atoms are important in regulating redox potential (*41*, *42*), different hydrogen bond patterns may be an important factor in the difference between subclusters.

In the HiPIP iron-sulfur cluster, subcluster 1, which consists of Fe1, Fe2, S3, and S4, is largely responsible for electron storage (*28*). The position of the amide proton of Cys^{75} near the S3 atom is different in the reduced and oxidized states (fig. S7, A and B). This difference was also observed in our previous study (*32*). In the oxidized state, the amide proton and oxygen atom of Trp^{74}-Cys^{75} deviate by 18.8°

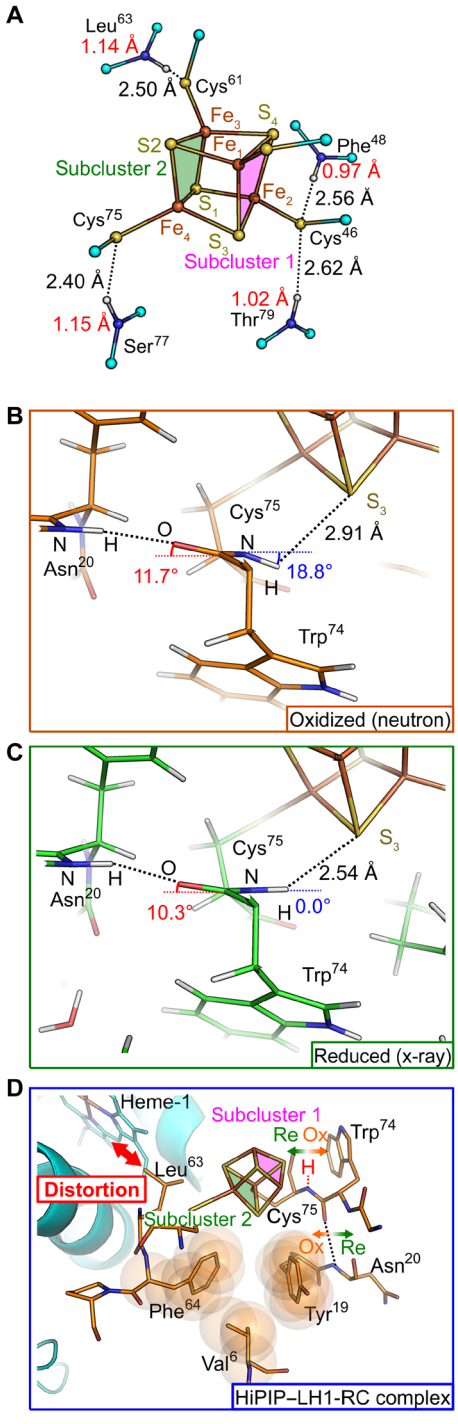

Fig. 4. Iron-sulfur cluster including hydrogen atoms. (**A**) Hydrogen bond with S_γ of cysteine residues covalently bound to Fe atoms. N—H bond lengths and H…O distances are shown in red and black, respectively. (**B**) Position of the amide proton of Cys^{75} in the oxidized state. The distance between the amide proton of Cys^{75} and S3 atom is shown in black. The deviations from the C_{i-1}—N_i—$C_{\alpha i}$ plane of the amide proton of Cys^{75} and oxygen of Trp^{74} are shown in blue and red, respectively. (**C**) Positions of the amide proton of Cys^{75} and oxygen of Trp^{74} in the reduced state [Protein Data Bank identifier (PDB ID) 5D8V]. (**D**) Structure of the HiPIP–LH1-RC complex around the contact surface between HiPIP and RC (PDB ID 7C52). The structural changes of the amide proton of Cys^{75} and the oxygen of Trp^{74} between the oxidized and reduced states are indicated by arrows.

and 11.7° from the C_{i-1}—N_i—$C_{\alpha i}$ plane, respectively (Fig. 4B). The amide proton of Cys^{75} is not oriented toward the S3 atom and shifts toward the indole ring of Trp^{74} because of the peptide bond distortion. The distance and angle between the amide proton of Cys^{75} and the center of the five-membered ring of Trp^{74} are consistent with the NH-π interaction (fig. S7C). This distance and angle are reasonable for obtaining the energetic stability due to the NH-π interaction (*43*). In contrast, in the reduced state, the amide proton of Cys^{75} is oriented toward the S3 atom (Fig. 4C). In the reduced state, the iron-sulfur cluster has one more electron than in the oxidized state; therefore, the amide proton of Cys^{75} is attracted by the S3 atom in subcluster 1. The structure of the HiPIP–LH1-RC complex has been reported (*44*). Heme-1 of LH1-RC is distorted by the interaction of Leu^{63} of HiPIP (Fig. 4D). Heme-1 receives electrons directly although its redox potential is lower than that of HiPIP (*45*). Because heme-1 is distorted by Leu^{63} and buried in a hydrophobic environment by complex formation, the redox potential increases, and the energy gap with HiPIP decreases (*44*). Phe^{64}, which is the next residue of Leu^{63} that interacts directly with heme-1, interacts with Val^6 and Tyr^{19} via its side chains (Fig. 4D). Consequently, the position of the amide proton of Asn^{20} changes, affecting the direction of the oxygen atom of Trp^{74}. The propagation of the structural change by the complex formation of HiPIP and LH1-RC probably leads to the orientation change of the amide proton of Cys^{75} that interacts with the S3 atom of the iron-sulfur cluster (Fig. 4D). The change in the electron storage capacity of the S3 atom located on the distal side of the binding surface will reduce the redox potential of HiPIP and facilitate the electron transfer from HiPIP to LH1-RC.

MATERIALS AND METHODS

Preparing the large crystal of oxidized HiPIP

HiPIP was extracted from *T. tepidum* and purified as reported previously (*28*, *31*, *32*). The purified HiPIP was oxidized with 10 mM potassium ferricyanide and concentrated to 18 mg/ml in 20 mM tris-HCl (pH 8.0). The crystals were obtained in a solution that was a 1:1 mixture of protein solution and reservoir solution (1.8 M ammonium sulfate and 0.1 M Na citrate buffer, pH 4.5) by the vapor diffusion method at 20°C. Large crystals for the neutron diffraction study were obtained by macroseeding using the vapor diffusion method at 20°C. The buffer of the purified sample was exchanged for the deuterium buffer (20 mM tris-DCl in D_2O) by ultrafiltration. The single crystal (about 0.5 mm by 0.1 mm by 0.1 mm) was transferred to a solution consisting of a 500-μl aliquot of the purified protein solution (4.5 mg/ml) with 1.7 M deuterated ammonium sulfate (D8) and 0.1 M Na citrate buffer (pD 4.5) in D_2O. The reservoir solution was a 1-ml aliquot of 1.7 M deuterated ammonium sulfate (D8) and 0.1 M Na citrate buffer (pD 4.5) in D_2O. The crystals with typical dimensions of 2.0 mm by 1.0 mm by 0.5 mm were obtained within 3 to 6 months.

Neutron and x-ray diffraction data collection

The crystal was flash-cooled in a nitrogen gas stream with a cryobuffer that consisted of reservoir solution with 20% (v/v) deuterated glycerol (D8). The time-of-flight neutron diffraction data were collected at 100 K using a neutron diffractometer (iBIX) at BL03 of the Materials and Life Science Experimental Facility at Japan Proton Accelerator Research Complex (J-PARC) (Tokai, Japan) (*46*, *47*). A total of 28 datasets was collected using wavelengths of 2.00 to 4.40 Å. The exposure time for each dataset was 8.5 hours at a beam power of 200 kW. The neutron diffraction data were processed using the program STARGazer (*48*, *49*). The −3σ cutoff was applied to remove the strongly negative intensities. The same crystal was also used for the cryogenic x-ray diffraction data collection using an Q315r detector [Area Detector Systems Corporation (ADSC), Poway, CA] at BL5A of the Photon Factory (Tsukuba, Japan). The x-ray diffraction data were processed and scaled using the program HKL2000 (*50*). Two datasets for high- and low-resolution regions were merged into a complete dataset.

Structure refinement

The structure of HiPIP was solved by the molecular replacement method using the oxidized HiPIP [Protein Data Bank identifier (PDB ID) 5WQQ] as a search model with the program MOLREP (*51*). The output structures were manually improved with the program Coot (*52*). The initial refinement of x-ray data was performed by the program Phenix (*53*) at 1.2-Å resolution. Then, the refinements with anisotropic atomic displacement parameters were performed using the program SHELXL (*54*) at 0.66-Å resolution. The coordinates and occupancies were refined with geometry restraints using the standard values in SHELXL. After the high-resolution x-ray data refinement, the neutron structure refinement was performed using the program Phenix. The refinement parameters of heavy atoms (C, N, O, S, and Fe) were fixed. The coordinates of the amide protons that had occupancies more than or equal to 0.60 that of deuterium or 0.75 that of protium and the deuterium atoms of the side chains in a single conformation were refined without geometry restraints. All figures for the molecular models were prepared using the program PyMOL (The PyMOL Molecular Graphics System, version 2.4.0a0; Schrödinger LLC).

SUPPLEMENTARY MATERIALS

Supplementary material for this article is available at https://science.org/doi/10.1126/sciadv.abn2276

View/request a protocol for this paper from *Bio-protocol*.

REFERENCES AND NOTES

1. L. Pauling, R. B. Corey, H. R. Branson, The structure of proteins: Two hydrogen-bonded helical configurations of the polypeptide chain. *Proc. Natl. Acad. Sci.* **37**, 205–211 (1951).
2. R. M. Smith, D. E. Hansen, The pH-rate profile for the hydrolysis of a peptide bond. *J. Am. Chem. Soc.* **120**, 8910–8913 (1998).
3. L. Pauling, R. B. Corey, Configurations of polypeptide chains with favored orientations around single bonds. *Proc. Natl. Acad. Sci.* **37**, 729–740 (1951).
4. D. Bordo, P. Argos, The role of side-chain hydrogen bonds in the formation and stabilization of secondary structure in soluble proteins. *J. Mol. Biol.* **243**, 504–519 (1994).
5. N. Eswar, C. Ramakrishnan, Secondary structures without backbone: An analysis of backbone mimicry by polar side chains in protein structures. *Protein Eng.* **12**, 447–455 (1999).
6. A. E. Mirsky, L. Pauling, On the structure of native, denatured, and coagulated proteins. *Proc. Natl. Acad. Sci.* **22**, 439–447 (1936).
7. C. N. Pace, H. Fu, K. L. Fryar, J. Landua, S. R. Trevino, D. Schell, R. L. Thurlkill, S. Imura, J. M. Scholtz, K. Gajiwala, J. Sevcik, L. Urbanikova, J. K. Myers, K. Takano, E. J. Hebert, B. A. Shirley, G. R. Grimsley, Contribution of hydrogen bonds to protein stability. *Protein Sci.* **23**, 652–661 (2014).
8. S. Y. Sheu, D. Y. Yang, H. L. Selzle, E. W. Schlag, Energetics of hydrogen bonds in peptides. *Proc. Natl. Acad. Sci. U.S.A.* **100**, 12683–12687 (2003).
9. J. U. Bowie, Membrane protein folding: How important are hydrogen bonds? *Curr. Opin. Struct. Biol.* **21**, 42–49 (2011).
10. S. Rajagopal, S. Vishveshwara, Short hydrogen bonds in proteins. *FEBS J.* **272**, 1819–1832 (2005).
11. B. S. Avvaru, C. U. Kim, K. H. Sippel, S. M. Gruner, M. Agbandje-McKenna, D. N. Silverman, R. McKenna, A short, strong hydrogen bond in the active site of human carbonic anhydrase II. *Biochemistry* **49**, 249–251 (2010).

12. C. N. Pace, Energetics of protein hydrogen bonds. *Nat. Struct. Mol. Biol.* **16**, 681–682 (2009).
13. L. Nisius, S. Grzesiek, Key stabilizing elements of protein structure identified through pressure and temperature perturbation of its hydrogen bond network. *Nat. Chem.* **4**, 711–717 (2012).
14. C. L. Worth, T. L. Blundell, Satisfaction of hydrogen-bonding potential influences the conservation of polar sidechains. *Proteins* **75**, 413–429 (2009).
15. D. S. Berkholz, C. M. Driggers, M. V. Shapovalov, R. L. Dunbrack Jr., P. A. Karplus, Nonplanar peptide bonds in proteins are common and conserved but not biased toward active sites. *Proc. Natl. Acad. Sci. U.S.A.* **109**, 449–453 (2012).
16. A. E. Brereton, P. A. Karplus, On the reliability of peptide nonplanarity seen in ultra-high resolution crystal structures. *Protein Sci.* **25**, 926–932 (2016).
17. R. Improta, L. Vitagliano, L. Esposito, Peptide bond distortions from planarity: New insights from quantum mechanical calculations and peptide/protein crystal structures. *PLOS ONE* **6**, e24533 (2011).
18. L. Esposito, A. De Simone, A. Zagari, L. Vitagliano, Correlation between ω and ψ dihedral angles in protein structures. *J. Mol. Biol.* **347**, 483–487 (2005).
19. Y. Fukuda, Y. Hirano, K. Kusaka, T. Inoue, T. Tamada, High-resolution neutron crystallography visualizes an OH-bound resting state of a copper-containing nitrite reductase. *Proc. Natl. Acad. Sci. U.S.A.* **117**, 4071–4077 (2020).
20. T. S. Ulmer, B. E. Ramirez, F. Delaglio, A. Bax, Evaluation of backbone proton positions and dynamics in a small protein by liquid crystal NMR spectroscopy. *J. Am. Chem. Soc.* **125**, 9179–9191 (2003).
21. B. Vögeli, How uniform is the peptide plane geometry? A high-accuracy NMR study of dipolar Cα–C′/HN–N cross-correlated relaxation. *J. Biomol. NMR* **50**, 315–329 (2011).
22. M. P. Blakeley, S. S. Hasnain, S. V. Antonyuk, Sub-atomic resolution X-ray crystallography and neutron crystallography: Promise, challenges and potential. *IUCrJ.* **2**, 464–474 (2015).
23. B. Schoepp, P. Parot, L. Menin, J. Gaillard, P. Richaud, A. Verméglio, In vivo participation of a high potential iron-sulfur protein as electron donor to the photochemical reaction center of *Rubrivivax gelatinosus*. *Biochemistry* **34**, 11736–11742 (1995).
24. H. A. Heering, Y. B. M. Bulsink, W. R. Hagen, T. E. Meyer, Influence of charge and polarity on the redox potentials of high-potential iron-sulfur proteins: Evidence for the existence of two groups. *Biochemistry* **34**, 14675–14686 (1995).
25. T. Glaser, I. Bertini, J. J. G. Moura, B. Hedman, K. O. Hodgson, E. I. Solomon, Protein effects on the electronic structure of the $[Fe_4S_4]^{2+}$ cluster in ferredoxin and HiPIP. *J. Am. Chem. Soc.* **123**, 4859–4860 (2001).
26. S. Niu, T. Ichiye, Insight into environmental effects on bonding and redox properties of [4Fe-4S] clusters in proteins. *J. Am. Chem. Soc.* **131**, 5724–5725 (2009).
27. A. Dey, F. E. J. Jenney Jr., M. W. W. Adams, E. Babini, Y. Takahashi, K. Fukuyama, K. O. Hodgson, B. Hedman, E. I. Solomon, Solvent tuning of electrochemical potentials in the active sites of HiPIP versus ferredoxin. *Science* **318**, 1464–1468 (2007).
28. Y. Hirano, K. Takeda, K. Miki, Charge-density analysis of an iron-sulfur protein at an ultra-high resolution of 0.48 Å. *Nature* **534**, 281–284 (2016).
29. T. Nogi, I. Fathir, M. Kobayashi, T. Nozawa, K. Miki, Crystal structures of photosynthetic reaction center and high-potential iron-sulfur protein from *Thermochromatium tepidum*: Thermostability and electron transfer. *Proc. Natl. Acad. Sci. U.S.A.* **97**, 13561–13566 (2000).
30. L. Liu, T. Nogi, M. Kobayashi, T. Nozawa, K. Miki, Ultrahigh-resolution structure of high-potential iron-sulfur protein from *Thermochromatium tepidum*. *Acta Crystallogr. D Biol. Crystallogr.* **58**, 1085–1091 (2002).
31. K. Takeda, K. Kusumoto, Y. Hirano, K. Miki, Detailed assessment of X-ray induced structural perturbation in a crystalline state protein. *J. Struct. Biol.* **169**, 135–144 (2010).
32. H. Ohno, K. Takeda, S. Niwa, T. Tsujinaka, Y. Hanazono, Y. Hirano, K. Miki, Crystallographic characterization of the high-potential iron-sulfur protein in the oxidized state at 0.8 Å resolution. *PLOS ONE* **12**, e0178183 (2017).
33. Y. Hanazono, K. Takeda, K. Miki, Characterization of perdeuterated high-potential iron-sulfur protein with high-resolution X-ray crystallography. *Proteins* **88**, 251–259 (2020).
34. L. Esposito, L. Vitagliano, A. Zagari, L. Mazzarella, Experimental evidence for the correlation of bond distances in peptide groups detected in ultrahigh-resolution protein structures. *Protein Eng.* **13**, 825–828 (2000).
35. A. Kvick, A. R. Al-Karaghouli, T. F. Koetzle, Deformation electron density of α-glycylglycine at 82 K. I. The neutron diffraction study. *Acta Crystallogr. B.* **B33**, 3796–3801 (1977).
36. L. Yao, B. Vögeli, J. Ying, A. Bax, NMR determination of amide N-H equilibrium bond length from concerted dipolar coupling measurements. *J. Am. Chem. Soc.* **130**, 16518–16520 (2008).
37. T. Steiner, Lengthening of the covalent X-H bond in heteronuclear hydrogen bonds quantified from organic and organometallic neutron crystal structures. *J. Phys. Chem. A* **102**, 7041–7052 (1998).
38. E. S. Feldblum, I. T. Arkin, Strength of a bifurcated H bond. *Proc. Natl. Acad. Sci. U.S.A.* **111**, 4085–4090 (2014).
39. N. W. Moriarty, D. Liebschner, D. E. Tronrud, P. D. Adams, Arginine off-kilter: Guanidinium is not as planar as restraints denote. *Acta Crystallogr. Sect. D Struct. Biol.* **76**, 1159–1166 (2020).
40. K. Yonezawa, N. Shimizu, K. Kurihara, Y. Yamazaki, H. Kamikubo, M. Kataoka, Neutron crystallography of photoactive yellow protein reveals unusual protonation state of Arg52 in the crystal. *Sci. Rep.* **7**, 9361 (2017).
41. Y. Zu, M. M. J. Couture, D. R. J. Kolling, A. R. Crofts, L. D. Eltis, J. A. Fee, J. Hirst, Reduction potentials of rieske clusters: Importance of the coupling between oxidation state and histidine protonation state. *Biochemistry* **42**, 12400–12408 (2003).
42. I. J. Lin, E. B. Gebel, T. E. Machonkin, W. M. Westler, J. L. Markley, Changes in hydrogen-bond strengths explain reduction potentials in 10 rubredoxin variants. *Proc. Natl. Acad. Sci. U.S.A.* **102**, 14581–14586 (2005).
43. J. Wang, L. Yao, Dissecting C–H···π and N–H···π interactions in two proteins using a combined experimental and computational approach. *Sci. Rep.* **9**, 20149 (2019).
44. T. Kawakami, L. J. Yu, T. Liang, K. Okazaki, M. T. Madigan, Y. Kimura, Z. Y. Wang-Otomo, Crystal structure of a photosynthetic LH1-RC in complex with its electron donor HiPIP. *Nat. Commun.* **12**, 1104 (2021).
45. F. Drepper, T. Saito, M. Kobayashi, T. Nozawa, P. Mathis, Electron transfer reactions of high-potential cytochromes in the reaction centre of *Chromatium tepidum*. *Photosynth. Res.* **55**, 325–330 (1998).
46. I. Tanaka, K. Kusaka, T. Hosoya, N. Niimura, T. Ohhara, K. Kurihara, T. Yamada, Y. Ohnishi, K. Tomoyori, T. Yokoyama, Neutron structure analysis using the IBARAKI biological crystal diffractometer (iBIX) at J-PARC. *Acta Crystallogr. D Biol. Crystallogr.* **66**, 1194–1197 (2010).
47. K. Kusaka, T. Hosoya, T. Yamada, K. Tomoyori, T. Ohhara, M. Katagiri, K. Kurihara, I. Tanaka, N. Niimura, Evaluation of performance for IBARAKI biological crystal diffractometer iBIX with new detectors. *J. Synchrotron Radiat.* **20**, 994–998 (2013).
48. T. Ohhara, K. Kusaka, T. Hosoya, K. Kurihara, K. Tomoyori, N. Niimura, I. Tanaka, J. Suzuki, T. Nakatani, T. Otomo, S. Matsuoka, K. Tomita, Y. Nishimaki, T. Ajima, S. Ryufuku, Development of data processing software for a new TOF single crystal neutron diffractometer at J-PARC. *Nucl. Instrum. Methods Phys. Res. A* **600**, 195–197 (2009).
49. N. Yano, T. Yamada, T. Hosoya, T. Ohhara, I. Tanaka, N. Niimura, K. Kusaka, Status of the neutron time-of-flight single-crystal diffraction data-processing software *STARGazer*. *Acta Crystallogr. D Struct. Biol.* **74**, 1041–1052 (2018).
50. Z. Otwinowski, W. Minor, Processing of X-ray diffraction data collected in oscillation mode. *Methods Enzymol.* **276**, 307–326 (1997).
51. A. Vagin, A. Teplyakov, *MOLREP*: An automated program for molecular replacement. *J. Appl. Cryst.* **30**, 1022–1025 (1997).
52. P. Emsley, B. Lohkamp, W. G. Scott, K. Cowtan, Features and development of *Coot*. *Acta Crystallogr. D Biol. Crystallogr.* **66**, 486–501 (2010).
53. D. Liebschner, P. V. Afonine, M. L. Baker, G. Bunkoczi, V. B. Chen, T. I. Croll, B. Hintze, L. W. Hung, S. Jain, A. J. McCoy, N. W. Moriarty, R. D. Oeffner, B. K. Poon, M. G. Prisant, R. J. Read, J. S. Richardson, D. C. Richardson, M. D. Sammito, O. V. Sobolev, D. H. Stockwell, T. C. Terwilliger, A. G. Urzhumtsev, L. L. Videau, C. J. Williams, P. D. Adams, Macromolecular structure determination using X-rays, neutrons and electrons: Recent developments in *Phenix*. *Acta Crystallogr. D Struct. Biol.* **75**, 861–877 (2019).
54. G. M. Sheldrick, Crystal structure refinement with SHELXL. *Acta Crystallogr. C Struct. Chem.* **71**, 3–8 (2015).

Acknowledgments: We would like to express our gratitude to K. Kurihara and the beamline staff for help with data collection at BL03 of the J-PARC for neutron data (proposal numbers: 2013A0174 and 2014A0250) and BL5A of the Photon Factory for x-ray data (proposal number: 2013G122). **Funding:** This work was supported by the Photon and Quantum Basic Research Coordinated Development Program (to K.M.); Quantum Leap Flagship Program (Q-LEAP) JPMXS0120330644 (to T.T.) from the Ministry of Education, Culture, Sports, Science and Technology (MEXT); PRESTO JPMJPR17G7 (to Y.Hi.) from the Japan Science and Technology Agency (JST); and Grants-in-Aid for Scientific Research (C) JP20K06523 (to K.M.), for Research Activity Start-up JP25891030 (to Y.Hi.) and JP20K22642 (to Y.Ha.), and for Young Scientists (B) JP15K18494 (to Y.Hi.) from the Japan Society for the Promotion of Science (JSPS). **Author contributions:** Conceptualization: Y.Ha., Y.Hi., K.T., T.T., and K.M. Investigation: Y.Ha., Y.Hi., K.T., K.K., T.T., and K.M. Funding acquisition: Y.Ha., Y.Hi., T.T., and K.M. Project administration: T.T. and K.M. Supervision: T.T. and K.M. Visualization: Y.Ha. Writing (original draft): Y.Ha. Writing (review and editing): Y.Ha., Y.Hi., K.T., K.K., T.T., and K.M. **Competing interests:** The authors declare that they have no competing interests. **Data and materials availability:** The atomic coordinates and structure factors have been deposited in the PDB under the accession number 7VOS. All other data needed to evaluate the conclusions in the paper are present in the paper and/or the Supplementary Materials.

Submitted 12 November 2021
Accepted 5 April 2022
Published 20 May 2022
10.1126/sciadv.abn2276